RSC Advances

PAPER

View Article Online
View Journal | View Issue

Cite this: *RSC Adv.*, 2024, **14**, 8567

The effects of Sr-substitution in $Ba_2SmTi_2Nb_3O_{15}$ ceramics: structural study, optical properties, and complex impedance spectroscopy†

Karim. Chourti, * Ilyas. Jalafi, Amine. Bendahhou, Soufian El Barkany and Mohamed. Abou-Salama

Received 3rd January 2024
Accepted 6th March 2024

DOI: 10.1039/d4ra00068d

rsc.li/rsc-advances

Ceramics of $(Ba_{1-x}Sr_x)_2SmTi_2Nb_3O_{15}$, denoted as BS_xSTN (x = 0, 0.25 and 0.5), were synthesized by the conventional solid-state reactions route. The impact of Sr-substitution in $Ba_2SmTi_2Nb_3O_{15}$ ceramics on their structural, optical, and dielectric properties are investigated. The Rietveld method was employed to confirm the formation of tetragonal tungsten bronze with the *P4bm* space group, using X-ray diffraction data. The substitution of Ba by Sr resulted in a decrease in cell parameters, density, and the average crystallite size as determined by Scherrer's formula ranged from 29.4 to 32 nm. The compounds frequency-dependent dielectric properties were studied using complex impedance spectroscopy over a temperature range of 50 to 420 °C at different frequencies. Dielectric measurements revealed a high dielectric constant, and the compounds exhibited characteristics of diffuse ferroelectric behavior. As the Sr content increased, optical gap energy increases from 3.29 to 3.59 eV, diffusivity increased from 1.19 to 1.52, Curie temperature (T_c) decreased from 269 to 213 °C, and the dielectric loss at room temperature and 1 kHz significantly decreased from 3×10^{-3} to 7×10^{-4}. The correlation between (T_c) and the off-center cationic displacement of Ti/Nb in the octahedral Ti/NbO_6 was analyzed. Cole–Cole plots for each sample displayed a single semicircular arc, indicating the presence of a single relaxation process.

1. Introduction

The physical characteristics, including electrical, magnetic, optical, and dielectric properties, of materials featuring a tetragonal tungsten bronze (TTBs) structure have been thoroughly investigated. The standard formula for a TTB is $(A1)_2(A2)_4(C)_4(B1)_2(B2)_8O_{30}$.[1–6] The pentagonal sites (A2) with a coordination number of 15 are capable of accepting sizable cations, including alkaline earth elements. On the other hand, the square sites (A1) with a coordination number of 12 are designed to accommodate moderately sized cations, such as rare earth elements. The triangular sites (C), with a coordination number of 9, are well-suited for hosting smaller cations like Li^+.[7,8] The octahedral sites (B1) and (B2) are typically occupied by highly charged cations like Ti^{4+}, Ta^{5+}, and Nb^{5+}.[9–11] The ferroelectric ordering in these materials is influenced by two primary factors: (i) the tilting of BO_6 octahedra and (ii) the change in ionic radii of the (A) or (B) site ions.[12,13] As a result, numerous studies have been carried to modify the properties of materials with a TTB structure, based on these two factors.

Compounds with the formula $Ba_{4-x}Sr_xSmFe_{0.5}Nb_{9.5}O_{30}$ (x = 0, 1, 2, 3 and 4) have been identified as relaxor materials. The pronounced dielectric relaxation in these materials is attributed to the disorder of Ba/Sr cations in the (A) sites.[14] In our investigation of the $Sr_2Sm_{1-x}Nd_xTi_2Nb_3O_{15}$ solid solution, which exhibits a TTB structure with the space group *P4bm*. In this structure, large ions like Sr^{2+} occupy the pentagonal cavities (A2), medium-sized ions such as Sm^{3+} are located in the square sites (A1),[14,15] and Ti^{4+}/Nb^{5+} ions occupy the octahedral sites (B1 and B2), while the sites (C) with a coordinate number of 9 remain unoccupied. These compounds exhibit ferroelectric behavior, and the Curie temperature (T_C) gradually decreases from 332 °C for $Sr_2SmTi_2Nb_3O_{15}$ to 246 °C for $Sr_2NdTi_2Nb_3O_{15}$. This trend correlates with the center displacement of the cation Ti/Nb(1) in the (B1) site.[16] In another study, ceramics with the composition $(Sr_xBa_{1-x})_4Sm_2Fe_2Nb_8O_{30}$ (x = 0, 0.1, 0.2, 0.3, 0.4) were investigated. These ceramics undergo a transition from a paraelectric to a ferroelectric phase, and this transition is influenced by the difference in radius (Δr) between the A1 and A2-site cations.[17] Within the TTB structure, the substitution of specific cations with ions of different sizes and/or valences at the (A1), (A2) and/or (B) sites leads to the formation of either ferroelectric or relaxor-type materials.

Department of Chemistry, Laboratory of Molecular Chemistry, Materials and Environment, Faculty Multidisciplinary Nador, University Mohammed Premier, B.P. 300, Selouane, Nador 62700, Morocco. E-mail: chokarim@gmail.com; k.chourti@ump.ac.ma

† Electronic supplementary information (ESI) available. See DOI: https://doi.org/10.1039/d4ra00068d

The size of cations and their substitution ratio at different sites within the TTB structure significantly impact the dielectric properties and overall structure of these materials.[18–21] Solid solutions, derived from a ferroelectric compound, involve cation substitutions either on the site (A1), as demonstrated in $Ba_2NdTi_2Nb_3O_{15}$,[22,23] $Ba_2SmTi_2Nb_3O_{15}$,[24] and $Sr_4R_2Ti_4Nb_6O_{30}$ (R = Sm and Eu),[25] or on the (A2) site, as observed in $Sr_2NdTi_2Nb_3O_{15}$,[16] which shows ferroelectric behavior, and $Ba_2NdTi_2Nb_3O_{30}$ which exhibits relaxor behaviors.[26]

In their study, M. C. Stennett *et al.*[27] investigated TTB-type ferroelectrics with the formula $Ba_2MTi_2Nb_3O_{15}$, were M = La, Nd, Sm, Gd, Bi. The researchers explored different composition, including $Ba_2LaTi_2Nb_3O_{15}$ (with a transition temperature, T_m∼−80 °C), $Ba_2BiTi_2Nb_3O_{15}$ (T_m∼−100 °C), $Ba_2NdTi_2Nb_3O_{15}$ (T_m∼165 °C), $Ba_2SmTi_2Nb_3O_{15}$ (T_m∼250 °C), and $Ba_2GdTi_2Nb_3O_{15}$ (T_m∼320 °C). In this family of $Ba_2MTi_2Nb_3O_{15}$ phases, the Curie temperature increases as the size of the M cation decreases. This observation suggests that the transition temperature is influenced by the dimensions of the cations M in TTB structure. The existence of ferroelectricity in these niobates is attributed to the occurrence of spontaneous polarization This phenomenon is usually a result of niobium displacements from the barycenter of the Ti/NbO_6 octahedron formed by oxygen atoms.[28,29]

The objective of this study is to investigate the solid solution $(Ba_{1-x}Sr_x)_2SmTi_2Nb_3O_{15}$ (x = 0, 0.25, 0.5). The specific aims of the research are as follows: (i) to examine the structural evolution within the solid solution, observing any changes or variations in the crystal structure as the substitution ratio of Ba and Sr cations is modified in the pentagonal site (A2); (ii) to investigate the dielectric properties of these phases with a specific focus on enhancing the dielectric constant while simultaneously minimizing dielectric losses. These properties provide insights into the material's response to an electric field and its energy dissipation behavior. Moreover (iii) to establish relationships between the crystalline structure and the dielectric and optical properties.

2. Materials and methods

BS_0STN, $BS_{0.25}STN$ and $BS_{0.5}STN$ samples were prepared using the conventional solid-state reaction method. Reagent grade $BaCO_3$, $SrCO_3$, Sm_2O_3, TiO_2 and Nb_2O_5, all supplied by Aldrich chemical, and high purity ≥99.9%, were employed. The starting powders were ground in an agate mortar to ensure homogeneity and reduce grain size. Sm_2O_3 powder was pre-dried at 750 °C for half an hour to remove traces of water and carbon dioxide. The mixtures were calcined in alumina crucibles at 1350 °C for 12 hours in air. The heating and cooling rates during the calcination process were maintained at 5 °C min^{-1}. The fundamental chemical reaction for pure phase synthesis can be represented by:

$$2(1-x)BaCO_3 + 2xSrCO_3 + \frac{1}{2}Sm_2O_3 + \frac{3}{2}Nb_2O_5 + 2TiO_2 \rightarrow (Ba_{1-x}Sr_x)_2SmTi_2Nb_3O_{15} + 2CO_2$$

Table 1 Selected compositions for our investigation

x	Compositions	Formula
0	$Ba_2SmTi_2Nb_3O_{15}$	BS_0STN
0.25	$(Ba_{0.75}Sr_{0.25})_2SmTi_2Nb_3O_{15}$	$BS_{0.25}STN$
0.5	$(Ba_{0.5}Sr_{0.5})_2SmTi_2Nb_3O_{15}$	$BS_{0.5}STN$

After calcination, the obtained powders were mixed with organic binders, specifically polyvinyl alcohol (PVA). The resulting mixture was then pressed into pellets with a diameter of 12 mm and 2 mm in thickness, applying a pressure of approximately 98 MPa. Subsequently, the disks were sintered at a temperature of 1400 °C in air for a duration of 2 h. This sintering step was conducted to facilitate the densification and consolidation of the pellets.

The X-ray diffraction (XRD) analysis was conducted at room temperature using CuKα radiation (λ = 1.5406 Å) to determine the crystal structure of the synthesized phases. XRD data were collected in the 2θ range of 5° to 120°, with a step size of 0.02° and a scanning speed of 1° min^{-1}. This XRD analysis aimed to provide detailed information about the crystallographic characteristics of the synthesized materials.

The refinement of various parameters, including cell parameters, reduced coordinates, and thermal agitation coefficient, was conducted using the Jana 2006 software.[30] The calculations were carried out in the same way for all compositions investigated. The visualization of the crystal structure of ceramics was taken by VESTA software.[31] The average crystallite size was estimated for the strongest diffraction peak using the Scherrer equation.[32]

The UV-Shimadzu (1800) type of UV/visible spectrometer was utilized to examine the optical properties. For dielectric measurements, both surfaces of the pellets were coated with silver paste and annealed for 30 minutes at 300 °C to obtain good electrical contacts. The relative permittivity and dielectric losses were determined using a BioLogic impedance analyzer model MTZ-35. The measurements were conducted over a frequency range of 100 Hz to 1 MHz, and the furnace and sample temperatures were controlled using MT-lab software with a heating rate of 5 °C min^{-1}.

The compositions studied are presented in the Table 1.

3. Results and discussion

3.1. Structural study

The diffractograms obtained for the compositions (Fig. 1) were successfully indexed in the tetragonal crystal system with the space group *P4bm*. The diffraction peaks were matched with structural model ICDD_PDF#38-1329, representing the TTB compound of the $Ba_6Ti_2Nb_8O_{30}$ formulation, as the initial patterns. The refinement of the different variables such as reduced coordinates and thermal agitation coefficient U_{iso}, was conducted using the Rietveld method.[33] The calculations were consistently performed across all compositions. The shape of the X-ray diffraction peaks was approximated using the Pseudo Voigt function, expressed as $PV = \eta L + (1-\eta)G$, where η is the

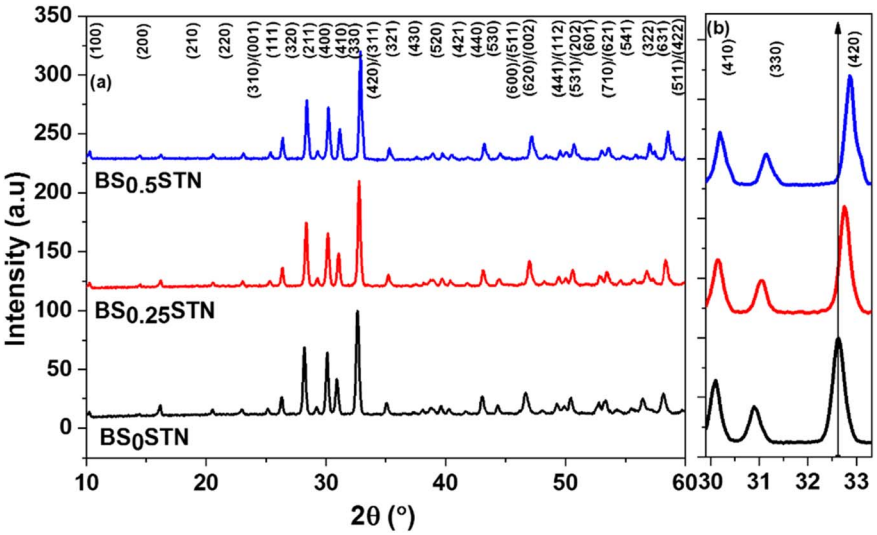

Fig. 1 (a) X-ray diffraction patterns of BS_xSTN powders, and (b) a shift of the diffraction peaks (410), (330) and (420).

mixing factor, G corresponds to the Gaussian function, and L represents the Lorentzian function.[34]

The peak shift in the XRD is based on the dopant size. If the dopant size is smaller Sr than the base metal Ba it occupies the interstitial position leading to change in the lattice structure and the d-spacing between the atoms become less and there is an increase in the X-ray diffraction resulting in higher angles. A decrease in peak intensity was observed as the Sr content increased (Fig. 1b). For certain reflection pairs, such as between (410) and (330), the difference in 2θ angles becomes more pronounced when compositions are rich in Ba. The shift of diffraction peaks towards higher angles corresponds to a reduction in the crystal lattice volume.

The replacement of Ba with Sr at the A2-site induces a shift of the diffraction peaks towards higher angles, indicating a decrease in the unit cell parameters. The obtained phases are pure, suggesting that the Sr element has diffused into the BS_x-STN lattice. The refined unit cell parameters and crystallite size for the BS_xSTN ceramics are provided in Table 2.

The refinement process was conducted within the *P4bm* space group. After several refinement cycles, the confidence factors, indicative of the refinement quality, stabilized within the following ranges: $4.3 \leq R_p \leq 5.4$, $5.9 \leq R_{wp} \leq 7.4$, and $2 \leq$ Gof ≤ 3.3. These values suggest a satisfactory agreement between the observed and calculated XRD patterns (Fig. 2a, and S1 in ESI†).

Table 2 shows that the lattice parameters a, c, and cell volume V decreased with the substitution rate the compounds. This trend can be attributed to the small difference between the ionic radii of barium ($r_{Ba}{}^{2+}$ with coordination number 15) = 1.65 Å, which is larger than strontium ($r_{Sr}{}^{2+}$ with coordination number 15) = 1.50 Å.[35] Additionally, the tetragonality $c/$

Table 2 Crystal structure parameters of BS_xSTN

Compounds	BS_0STN	$BS_{0.25}STN$	$BS_{0.5}STN$
$a = b$ (Å)	12.2778(8)	12.2598(7)	12.2242(8)
c (Å)	3.8980(3)	3.8711(3)	3.8540(3)
c/a	0.317	0.316	0.315
V (Å^3)	587.60(7)	581.83(6)	575.92(7)
Z	2	2	2
Crystallite size D (nm)	29.4	31.9	32.0
Profile function	Pseudo Voigt	Pseudo Voigt	Pseudo Voigt
u	1.4265	1.1666	1.2547
v	−0.7335	−0.5705	−0.7239
w	0.2061	0.1574	0.2058
CuKα radiation (Å)	1.5406	1.5406	1.5406
Measuring range 2θ (°)	5–120	5–120	5–120
Step 2θ (°)	0.02	0.02	0.02
Number of refined parameters	38	38	38
Goodness-of-fit (Gof)	2.84	2.71	2.26
R-profile (R_p) (%)	4.32	4.23	5.39
R-weighted profile (R_{wp}) (%)	5.85	5.85	7.40
Expected residual factor (R_{exp}) (%)	2.06	2.15	3.27

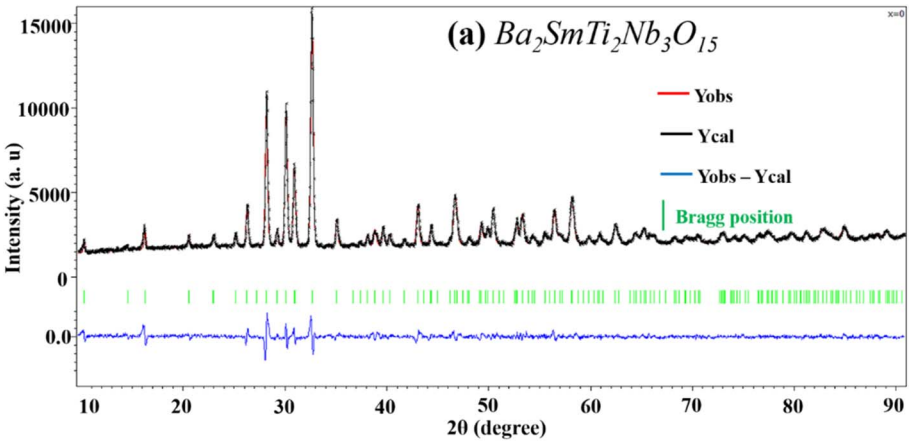

Fig. 2 X-ray diffraction refinement for BS_xSTN powders: (a) $x = 0$.

a decreased from 0.317 in undoped BS_0STN to 0.315 in $BS_{0.5}STN$, indicating a decrease in distortions with increasing substitution. The Table 3 shows the refinement of structural parameters for BS_xSTN.

In the BS_xSTN crystal structure, specific ions occupy different sites. Ba^{2+} and Sr^{2+} occupy the pentagonal sites (A2), Sm^{3+} occupy the square sites (A1), and Ti^{4+} and Nb^{4+} occupy the octahedral sites. The sites (C) in the structure remain unoccupied. Examining the $Ti/Nb(1)O_6$ octahedra reveals that the Ti/Nb(1)–O(1)′ bond length is consistently smaller than Ti/Nb(1)–O(1) across all compositions. In the $Ti/Nb(2)O_6$ octahedra, there are variations in the Ti/Nb(2)–O distances for all compositions, suggesting that the $Ti/Nb(2)O_6$ octahedra are more distorted or deformed compared to the $Ti/Nb(1)O_6$ octahedra, a common observation in TTB structures. In the square sites (A1), it has been noted that the Sm-O(3) distance increases

Table 3 Refinement of the structural parameters for BS_xSTN

Atom	Site	*x*	*y*	*z*	Occupancy	U_{iso}
BS_0STN						
Ba	4c	0.1708(2)	0.6708(2)	0.067(6)	1	0.025(16)
Sm	2a	0	0	0.020(6)	1	0.033(2)
Ti1/Nb1	2b	0	0.5	0.497(7)	0.4/0.6	0.004(4)
Ti2/Nb2	8d	0.0732(4)	0.2143(4)	0.538(6)	0.4/0.6	0.006(16)
O1	2b	0	0.5	0.134(19)	1	0.008(6)
O2	4c	0.2807(16)	0.7807(16)	0.484(17)	1	0.008(6)
O3	8d	0.063(2)	0.1935(18)	0.125(11)	1	0.008(6)
O4	8d	0.3493(17)	0.0044(13)	0.615(11)	1	0.008(6)
O5	8d	0.1308(17)	0.078(2)	0.615(10)	1	0.008(6)
$BS_{0.25}STN$						
Sr/Ba	4c	0.1706(3)	0.6706(3)	0.084(7)	0.25/0.75	0.024(19)
Sm	2a	0	0	0.021(7)	1	0.031(2)
Ti1/Nb1	2b	0	0.5	0.486(8)	0.4/0.6	0.001(4)
Ti2/Nb2	8d	0.0756(4)	0.2175(4)	0.544(7)	0.4/0.6	0.002(15)
O1	2b	0	0.5	−0.830(3)	1	0.013(7)
O2	4c	0.2826(16)	0.7826(16)	0.600(2)	1	0.013(7)
O3	8d	0.062(2)	0.1921(17)	0.088(15)	1	0.013(7)
O4	8d	0.3492(18)	0.0014(13)	0.642(13)	1	0.013(7)
O5	8d	0.1382(17)	0.076(2)	0.480(14)	1	0.013(7)
$BS_{0.5}STN$						
Sr/Ba	4c	0.1698(3)	0.6698(3)	0.036(6)	0.50/0.50	0.029(2)
Sm	2a	0	0	0.052(6)	1	0.027(2)
Ti1/Nb1	2b	0	0.5	0.587(8)	0.4/0.6	0.012(4)
Ti2/Nb2	8d	0.0764(4)	0.2159(4)	0.562(6)	0.4/0.6	0.003(16)
O1	2b	0	0.5	−0.025(17)	1	0.025(6)
O2	4c	0.289(2)	0.789(2)	0.475(15)	1	0.025(6)
O3	8d	0.068(3)	0.199(2)	−0.015(11)	1	0.025(6)
O4	8d	0.3453(18)	0.0001(16)	0.474(12)	1	0.025(6)
O5	8d	0.129(2)	0.082(2)	0.461(10)	1	0.025(6)

Table 4 Selected bond distances (Å) for composition BS_xSTN

Cation-O	Mul	BS_0STN	$BS_{0.25}STN$	$BS_{0.5}STN$
Environment of Sr/Ba				
Sr/Ba-O(3)	×2	3.2622(3)	2.8803(10)	3.2701(3)
	×2	3.4527(3)	3.7383(13)	3.2696(3)
Sr/Ba-O(4)	×2	3.0254(16)	2.6917(8)	2.8880(16)
	×2	2.7575(14)	3.1682(10)	2.7539(15)
Sr/Ba-O(5)	×2	3.4154(18)	2.7907(8)	3.3775(19)
	×2	2.9065(16)	3.5572(11)	3.0857(18)
Sr/Ba-O(2)	×1	2.9018(15)	2.8260(8)	2.8170(16)
	×1	2.7539(14)	2.9954(9)	2.6515(15)
Environment of Sm				
Sm-O(3)	×4	2.3315(15)	2.5588(9)	2.6316(2)
Sm-O(5)	×4	3.2470(18)	3.3025(7)	2.9357(16)
	×4	2.5317(13)	2.5520(11)	2.5704(14)
Environment of the octahedron $Ti/Nb(1)O_6$				
Ti/Nb(1)–O(1)	×1	2.2647(19)	2.1421(11)	2.1112(17)
Ti/Nb(1)–O(1)′	×1	1.7330(12)	1.7433(8)	1.7434(14)
Ti/Nb(1)–O(4)	×4	1.9109(12)	2.0433(7)	1.8539(14)
Environment of the octahedron $Ti/Nb(2)O_6$				
Ti/Nb(2)–O(2)	×1	1.9229(13)	1.8880(7)	1.9071(14)
Ti/Nb(2)–O(3)	×1	2.2628(17)	1.9370(9)	2.1148(17)
	×1	1.7679(13)	2.0611(9)	1.7614(14)
Ti/Nb(2)–O(4)	×1	1.8691(12)	1.7993(6)	1.8836(14)
Ti/Nb(2)–O(5)	×1	2.1773(14)	1.9900(6)	2.1608(16)
	×1	1.8926(12)	2.2305(7)	1.8308(14)

as the value of x increases. Conversely, for the pentagonal sites (A2), the Sr-O(5) distance rises with an increase in Ba content. As indicated in Table 4, all compositions exhibit centric displacements along the c-axis for both Ti and Nb cations within the $Ti/Nb(1)O_6$ and $Ti/Nb(2)O_6$ octahedra, as illustrated in Fig. 3b. Notably, the $Ti/Nb(1)O_6$ octahedra in all compositions display an O(1)–Nb/Ti(1)–O(1) bond angle of 180°, indicating a linear arrangement. Moreover, these octahedra manifest four equal Ti/Nb(1)–O(4) bond lengths, as detailed in Table 4.

Within the equatorial plane of the $Ti(1)O_6$ octahedron, the O–Ti(1)–O angles, spanning from approximately 74° to 105°,

Table 5 Selected bond angles for BS_xSTN

Angles (°)	BS_0STN	$BS_{0.25}STN$	$BS_{0.5}STN$
O(1)–Ti(1)–O(1)	180(0)	180(0)	180(0)
O(1)–Ti(1)–O(4)	102.191(12)	105.954(9)	92.372(3)
	77.808(12)	74.045(9)	87.627(3)
O(4)–Ti(1)–O(4)	155.617(3)	148.091(18)	175.254(6)
O(2)–Ti(2)–O(3)	96.599(17)	95.143(5)	92.757(8)
	110.002(10)	82.785(4)	98.432(4)
O(2)–Ti(2)–O(4)	89.789(0)	86.076(0)	95.970(0)
O(2)–Ti(2)–O(5)	161.655(17)	151.271(14)	172.084(9)
	86.889(3)	89.230(3)	90.211(0)
O(3)–Ti(2)–O(3)	150.249(3)	152.712(15)	167.864(13)
O(3)–Ti(2)–O(4)	87.735(14)	88.882(15)	89.817(4)
	104.941(0)	118.209(0)	93.655(0)
O(3)–Ti(2)–O(5)	66.377(0)	113.512(10)	81.438(5)
	70.456(10)	94.534(18)	93.777(10)
O(4)–Ti(2)–O(5)	157.368(3)	147.195(18)	169.537(7)

suggest a relatively lower degree of distortion for this type of octahedron. Furthermore, the O(1)–Ti/Nb(1)–O(1) angle of 180° suggests a rotation of the octahedra around the b-axis.

The angles formed by O(3)–Ti(2)–O(3)′ surpass 150° and demonstrate an upward trend with increasing values of x, suggesting an expansion of these angles with the substitution from Ba to Sr increases. This observation implies an increasing distortion in the $Ti(2)O_6$ octahedra as the composition undergoes changes. The diverse angles within the equatorial plane of the $Ti(2)O_6$ octahedron, detailed in Table 5, additionally affirm that this octahedron is more distorted compared to the $Ti(1)O_6$ octahedron.

Fig. 3a presents the crystallographic structure along the c-axis, depicting different sites such as pentagonal (A2), square (A1), triangular (C), and octahedral sites (B1, B2). The displacements of Ti/Nb(1) and Ti/Nb(2) cations within the Ti/NbO_6 octahedra are shown in Fig. 3b.

3.2. Density of ceramic samples

The ceramic samples' experimental density (ρ_{ex}) was measured using a KERN analytical balance based on Archimedes' method.

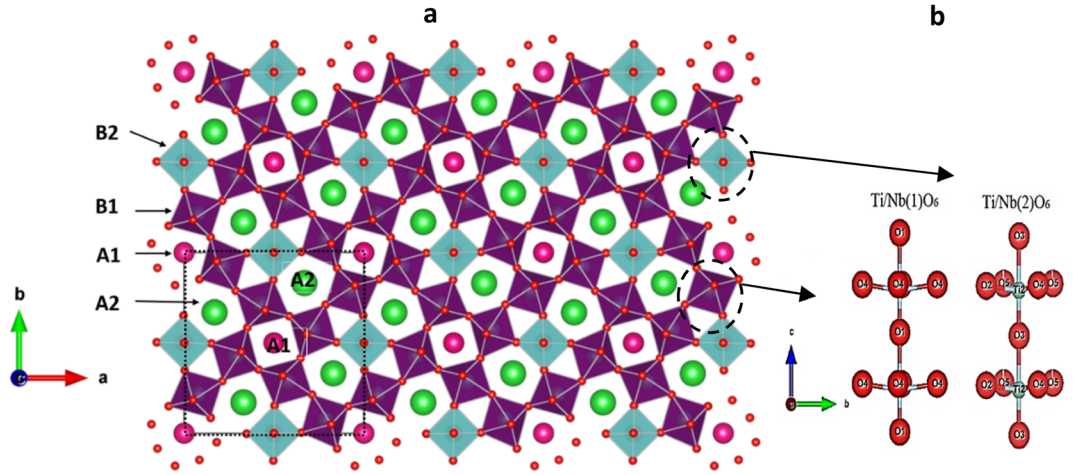

Fig. 3 (a) Representation of the TTB structure of BS_xSTN along the "c" axis. (b) Displacements of the Ti/Nb(1) and Ti/Nb(2) cations.

Table 6 ρ_{th}, ρ_{ex}, and ρ_r of BS_xSTN ceramics

Compounds	ρ_{th} (g cm^{-3})	ρ_{ex} (g cm^{-3})	ρ_r (%)
BS_0STN	5.84	5.43	92.9
$BS_{0.25}STN$	5.74	5.33	92.8
$BS_{0.5}STN$	5.70	5.31	93.1

The theoretical density (ρ_{th}) was calculated using lattice parameter values obtained from crystallographic data. And relative density (ρ_r) is the quotient obtained by diving the experimental density by theoretical density.[14,36] The obtained results are summarized in Table 6. This calculation enabled the assessment of compactness and the inference of material in porosity. The results indicate that with an increase in x, the density decreases, accompanied by an increase in porosity.

3.3. Optical properties

The optical transmittance spectrum for BS_0STN, $BS_{0.25}STN$, and $BS_{0.5}STN$ materials is presented in Fig. 4. Analysis of the spectra indicates that pure BS_0STN exhibits higher optical transmittance than both $BS_{0.25}STN$ and $BS_{0.5}STN$. The elevated optical transmittance might be a result of a reduced crystallite size in BS_0STN. The optical gap energy (E_g) of the compounds were calculated by applying the Tauc law, as expressed in eqn (1).[37]

$$(\alpha h\upsilon)^2 = C(h\upsilon - E_g), \alpha = \frac{\mathrm{Ln}(T)}{d} \quad (1)$$

In eqn (1), T represents the transmittance (%), d is the sample thickness, C is a constant, (E_g) signifies the optical energy band gap, υ is the light frequency, and h stands for Planck's constant. The direct optical band gap energy (E_g) is ascertained by extrapolating the linear segment of the plot depicting $(\alpha h\upsilon)^2$ *versus* ($h\upsilon$) to the point where $(\alpha h\upsilon)^2 = 0$, as depicted in Fig. 4. The computed optical band gap energies (E_g) for BS_0STN, $BS_{0.25}STN$, and $BS_{0.5}STN$ are 3.25 eV, 3.56 eV, and 3.59 eV, respectively. Our study's band gap values are consistent with the range reported in the literature, as indicated in ref. 38–40.

Firstly, a higher bandgap (E_g) means that electrons require greater energy or an elevated electric field to transition from the valence band to the conduction band. The increase in (E_g) from 3.25 to 3.59 eV with the rise in x suggests that the introduction of Sr into BSTN reduces the electron jump between these bands, potentially enhancing resistance to a higher applied electric field.[41] Secondly, consequently, an increase in the band gap was observed with the Sr doping rate, appears to be associated with the enlargement of crystallite size, as indicated in the studies.[42–45] Furthermore, the band gap[46,47] is enhanced in the presence of strontium.

3.4. Study of dielectric properties

Indeed, the investigation of the dielectric properties of BS_xSTN ceramics is crucial for gaining insights into their electrical behavior. It allows for establishing a correlation between the dielectric properties and the material's structure, providing valuable information about the material's electrical characteristics.

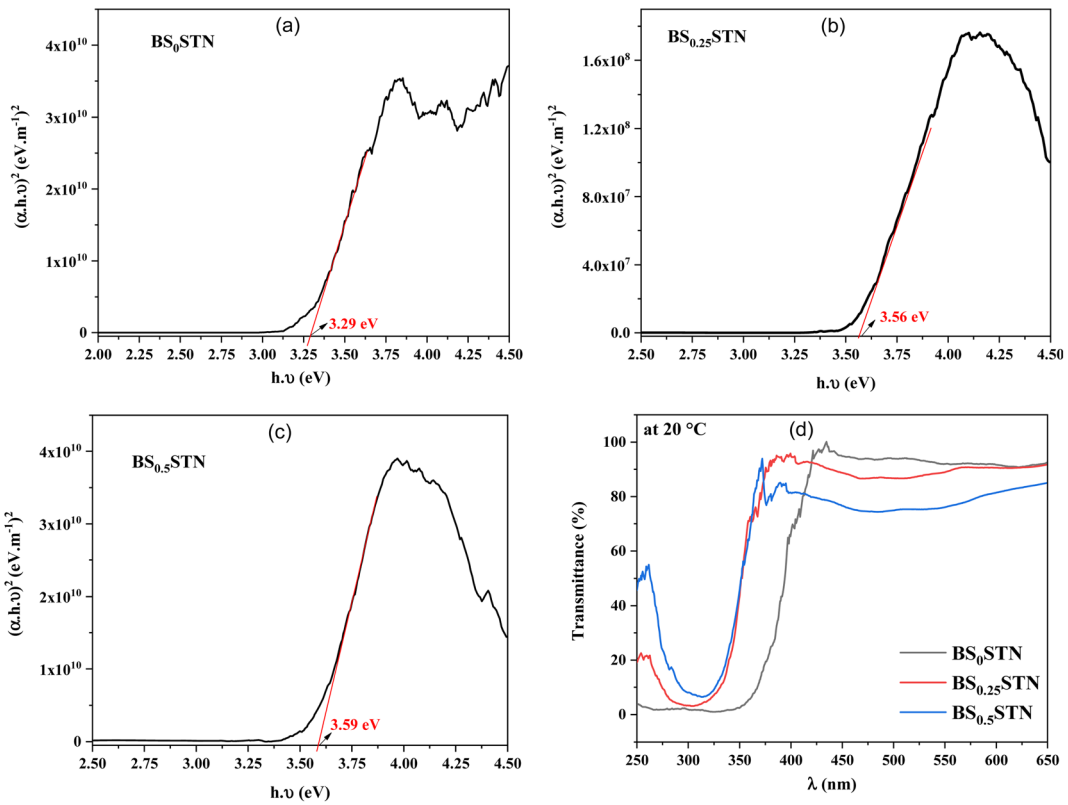

Fig. 4 The $(\alpha h\upsilon)^2$ *vs.* ($h\upsilon$) of BS_xSTN, where: (a) $x = 0$, (b) $x = 0.25$, (c) $x = 0.5$, and (d) optical transmittance spectrum.

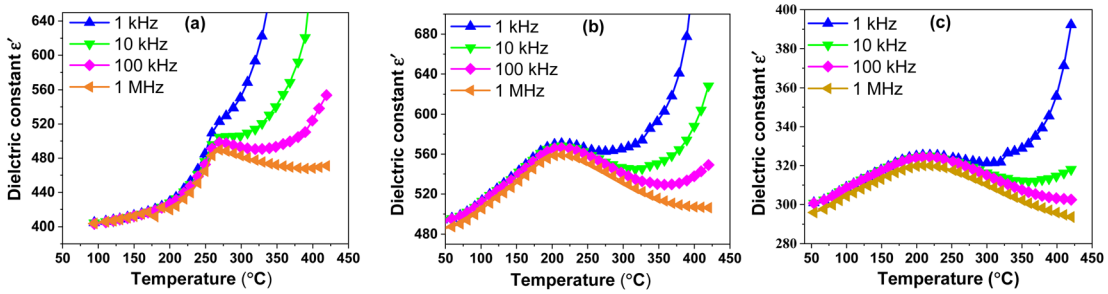

Fig. 5 Thermal evolution of the dielectric constant ε' of BS_xSTN as a function of temperatures at different frequencies: (a) $x = 0$, (b) $x = 0.25$, and (c) $x = 0.50$.

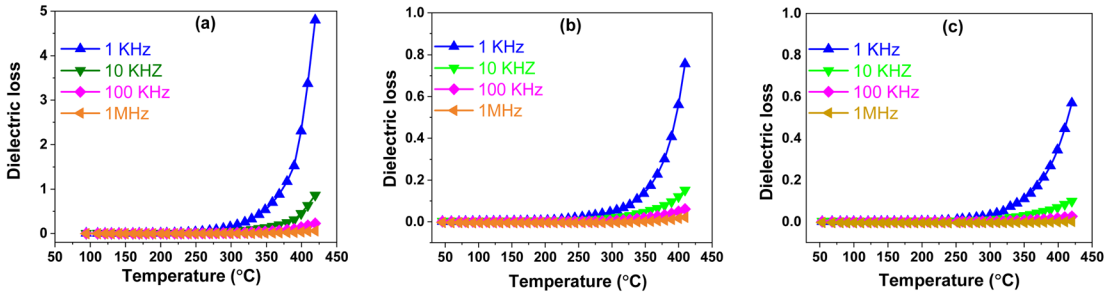

Fig. 6 The thermal evolution of the dielectric loss for BS_xSTN as a function of temperature at different frequencies: (a) $x = 0$, (b) $x = 0.25$, and (c) $x = 0.5$.

3.4.1. Dielectric constant (ε'). Fig. 5 shows the variation of the dielectric constant as a function of the temperatures (50 °C–420 °C) at different frequencies (1 kHz–1 MHz) for the BS_xSTN ceramics. The graph reveals a notable a dielectric anomaly in all compounds, characterized by a large maximum in the dielectric constant. This anomaly indicates the presence of a diffuse ferroelectric phase transition in the materials. Interestingly, all compounds have the same transition temperature (T_C) across the entire frequency range investigated. The T_C values decreased and are approximately 269 °C, 218 °C, and 213 °C for BS_0STN, $BS_{0.25}STN$, and $BS_{0.5}STN$ samples, respectively.

The variation in the maximum values of the dielectric constant (ε'_{max}) with Sr content in the BS_xSTN ceramics suggests that the substitution of Ba by Sr in the pentagonal site (A2) influences the dielectric behavior of the materials. The dielectric constant maximum values for BS_xSTN ceramics at the Curie temperature and 1 MHz are as follows: 489.65 (BS_0STN), 559.23 ($BS_{0.25}STN$), and 319.96 ($BS_{0.5}STN$). The minimum value of ε'_{max} is observed for $BS_{0.5}STN$, indicating that the substitution of Ba with Sr in the (A2) site leads to a decrease in the dielectric constant. This trend can be attributed to the influence of ionic radius. The larger ionic radius of Sr compared to Ba could lead to increased distortions or changes in the local coordination environments around the (A2) sites. This observation suggests that the dielectric properties of the BS_xSTN ceramics are relatively sensitive to the Sr content. The higher ε' value at low frequencies confirms the presence of various types of polarization, whereas at high frequencies, it is primarily attributed to electronic polarization. With increasing frequency, the dielectric permittivity may start to decrease, and the constant at 1 kHz is higher than that at 1 MHz. This could be attributed to phenomena such as partial reorientation of dipoles that cannot rapidly follow the electric field due to the higher frequency.[48]

The Curie temperature T_C decreases with the increase of x, reaching a minimum value of 213 °C for the $BS_{0.5}STN$ composition. This change in Tc may be attributed to the influence of a slight displacement of Ti/Nb(1) cations along the c-axis, specifically indicated by the (O(1)–Ti/Nb(1)–O(1)′) in the Ti/NbO_6 octahedra. This displacement is associated with alterations in the Ti/Nb(1)–O(1)′ bond distance, which inversely varies with the Ti/Nb(1)–O(1) distance (as shown in Table 4).

In ferroelectric materials, the ferroelectric ⇔ paraelectric transition is accompanied by a structural change. Below the transition temperature T_C, the corresponding space group is *P4bm* (non-centrosymmetric and polar). Conversely, above T_C, the structure often corresponds to *P4/mbm* (centrosymmetric and non-polar). It can be seen that the dielectric properties were closely related to the structure.

3.4.2. Dielectric loss (tan δ). In Fig. 6, the temperature-dependent evolution of dielectric loss for BS_xSTN is presented, measured at different frequencies (1 kHz–1 MHz) as a function of temperature (50 °C–420 °C). It is obviously observed that the BS_xSTN ceramics exhibit low dielectric loss, which decreases with the increasing Sr content. The tangent losses appear to remain constant and start increasing after 300 °C. At room temperature and 1 kHz, the dielectric loss values are observed to be 3×10^{-3}, 1×10^{-3}, and 0.7×10^{-3} for different compositions, respectively. Remarkably, the dielectric loss

Table 7 Comparison of dielectric constant (ε'), dielectric loss (tan δ), maximum values of permittivity (ε'_{max}), and Curie temperature (T_C) at a frequency of 1 MHz and room temperature (RT) of some type TTBs in previous literature

Composition	ε' (at RT)	Tan δ (at RT)	ε'_{max} (at T_C)	T_C (°C)	Ref.
$Ba_4Sm_2Ti_4Ta_6O_{30}$	159.6	3.5×10^{-3}	—	—	49
$Ba_3Sm_3Ti_5Ta_5O_{30}$	134.4	4.6×10^{-3}	—	—	49
$Sr_4Eu_2Ti_4Nb_6O_{30}$	125	50×10^{-3}	210	402	50
$Sr_5EuTi_3Nb_7O_{30}$	230	25×10^{-3}	360	245	50
$Ba_2NdTi_2Ta_3O_{15}$	136.9	0.7×10^{-3}	—	—	51
$Ba_3Nd_3Ti_5Ta_5O_{30}$	103.1	8.8×10^{-3}	—	—	51
$Ba_5NdTi_3Ta_7O_{15}$	162.4	1.3×10^{-3}	—	—	51
$Sr_2NdTi_2Nb_3O_{15}$	106.4	2.7×10^{-3}	127	246	16
$Sr_2SmTi_2Nb_3O_{15}$	142.3	1.3×10^{-3}	194	332	16
$(Ba_{0.5}Sr_{0.5})_2SmTi_2Nb_3O_{15}$	295.8	0.7×10^{-3}	319.9	213	This work
$(Ba_{0.75}Sr_{0.25})_2SmTi_2Nb_3O_{15}$	570.6	1×10^{-3}	559.2	218	This work
$Ba_2SmTi_2Nb_3O_{15}$	403.8	3×10^{-3}	489.6	269	This work

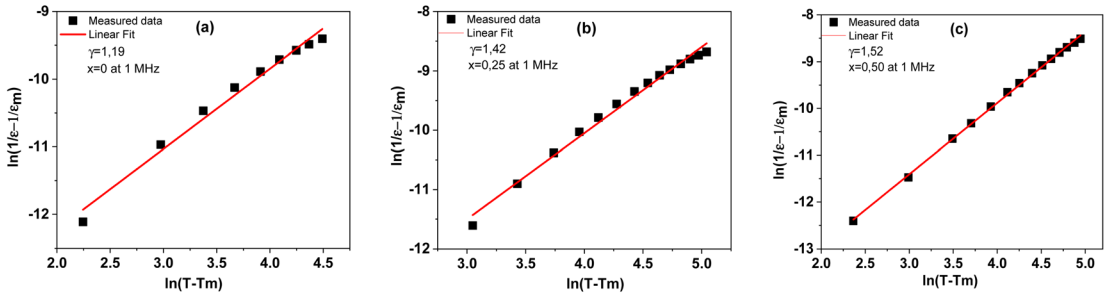

Fig. 7 Plots of $\ln\left(\frac{1}{\varepsilon'}-\frac{1}{\varepsilon'_{max}}\right)$ as a function of $\ln(T - T_{max})$ at 1 MHz for the BS_xSTN ceramics: (a) $x = 0$, (b) $x = 0.25$, and (c) $x = 0.5$. The solid lines represent the linear fitted results.

values vary with the Sr content x, reaching a minimum of 0.7×10^{-3} for $BS_{0.5}STN$. This behavior is attributed to the substitution of Ba by Sr in the pentagonal (A2) site. The dielectric loss tan δ, increases with the rise in temperature, leading to a subsequent significant loss, possibly due to the increase in electrical conductivity.

Table 7 provides an overview of the dielectric characteristics of some TTBs. After comparing different types of TTB ceramics, it is observed that $Ba_2SmTi_2Nb_3O_{15}$ displays a higher dielectric constant ε' and lower dielectric loss, indicating favorable results in comparison to Ba-based TTBs such as $Ba_4Sm_2Ti_4Ta_6O_{30}$ and $Ba_3Nd_3Ti_5Ta_5O_{30}$.

3.4.3. Diffuse phase transition. The diffuse phase transition behavior of the dielectric constant can be evaluated using the modified Curie–Weiss eqn (2):[52,53]

$$\ln\left(\frac{1}{\varepsilon'}-\frac{1}{\varepsilon'_{max}}\right) = \gamma \ln(T - T_{max}) + C \quad (2)$$

In this equation, ε' represents the dielectric constant, ε'_{max} is the peak value of ε' at T_{max}, C is the modified Curie–Weiss constant, and γ is the diffusivity exponent. Fig. 7 shows the variation of $\ln\left(\frac{1}{\varepsilon'}-\frac{1}{\varepsilon'_{max}}\right)$ with $\ln(T - T_{max})$ at 1 MHz for BS_xSTN. The diffusivity exponent values are determined by analyzing the slopes of individual curves, and these calculated values are then displayed in Table 8. The γ values range from 1 to 2, signifying a spectrum of ferroelectric behaviors. A γ value of 1 corresponds to a typical ferroelectric behavior in accordance with the Curie–Weiss law, while a γ value of 2 indicates a shift towards relaxation and a fully disordered ferroelectric system.[54] This suggests a diffuse ferroelectric nature of the BS_xSTN ceramics. The γ values indicate that the materials possess disorder. Furthermore, the increasing values of γ with Sr content suggest an increase in diffusivity.

Table 8 The values of diffusivity γ at 1 MHz of the solid solution BS_xSTN

Compounds	BS_0STN	$BS_{0.25}STN$	$BS_{0.5}STN$
γ	1.19	1.45	1.52

The diffuse nature of the phase transition in BS_xSTN ceramics is suggested to be attributed to the presence of oxygen vacancies.[55] In oxide materials, oxygen vacancies can easily be formed in oxide materials by the loss of oxygen from the crystal lattice, especially during heating at elevated temperatures (typically above 1300 °C).[56] The Kröger–Vink notation provides a useful tool for understanding the occurrence of oxygen vacancies:

$$O_O \rightarrow \frac{1}{2}O_2 \uparrow + V_O^{\cdot\cdot} + 2e^-$$

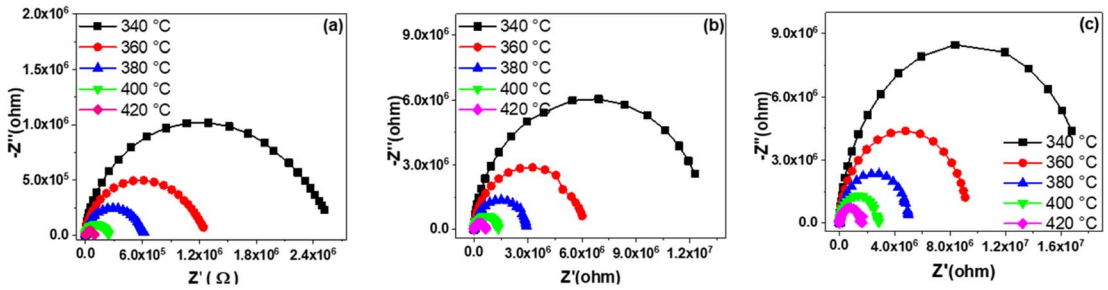

Fig. 8 The variation of the imaginary part-Z'' of impedance as a function of the real part Z' at different temperatures for BS_xSTN: (a) $x = 0$, (b) $x = 0.25$, and (c) $x = 0.5$.

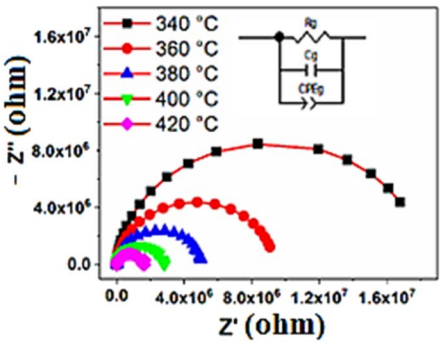

Fig. 9 Adjusted Nyquist diagram for the $BS_{0.5}STN$ composition at different temperatures. The solid red lines show the adjusted data with the ZView software.

Indeed, the presence of oxygen vacancies ($V_O^{\cdot\cdot}$) within the system can induce disorder and contribute to a diffuse-type ferroelectric-paraelectric phase transition.[57]

3.5. Complex impedance analysis (CIA)

Fig. 8 represents the variation of the imaginary part (Z'') of impedance as a function of the real part (Z') at different temperature. As depicted in the figure, an increase in temperature leads to a reduction in the size of the semicircle in the Cole–Cole plot for each sample, indicating a gradual decrease in compound resistance. The resistance values exhibit an increase ranging from 0.24×10^6 Ω for BS_0STN to 2.747×10^6 Ω for $BS_{0.5}STN$ with the substitution rate. The observed arc corresponds to the grain response in the high-frequency range. In according with the brick model,[58] the electrical properties of BS_xSTN ceramics are well correlated with the internal microstructure.

In order to extract the electrical properties of the materials, we employed an equivalent electrical circuit using the Zview 2.8d program, as shown in Fig. 9. The electrical model comprises the RQC circuit, associated to the grain contribution, grain resistance (R_g), grain capacitance (C_g), and the constant phase element (CPE). The introduction of the constant phase element is necessary to account for the non-ideal capacitive behavior observed in the circuit. This non-ideal grain behaviour may be due to the presence of more than one relaxation process.[59]

The constant phase element "Q" is calculated using the following expression in eqn (3):[60,61]

$$C = (R^{1-\alpha}Q)^{1/\alpha} \quad (3)$$

For an ideal resistor and capacitor, the values of "α" are respectively zero and one.[62] The good of agreement between the experimental data represented in points, and the theoretical values represented by the red line enables the validation of the proposed equivalent circuit (see Fig. 9). The different parameters employed for adjustments are displayed in Table 9.

Table 9 Electrical parameters of equivalent circuits for BS_xSTN ceramics

Compounds	T (°C)	R_g (MΩ)	C_g (nF)	Q_g (nF $s^{\alpha-1}$)	α
BS_0STN	340	2.629	0.177	2.138	0.606
	360	1.264	0.173	2.196	0.637
	380	0.620	0.168	2.396	0.660
	400	0.243	0.152	3.152	0.679
$BS_{0.25}STN$	340	13.21	0.186	0.255	0.759
	360	6.274	0.175	0.195	0.833
	380	2.959	0.170	0.251	0.832
	400	1.349	0.157	0.290	0.857
$BS_{0.5}STN$	340	19.20	0.175	0.134	0.776
	360	9.486	0.175	0.254	0.713
	380	5.093	0.172	0.261	0.733
	400	2.765	0.168	0.218	0.778

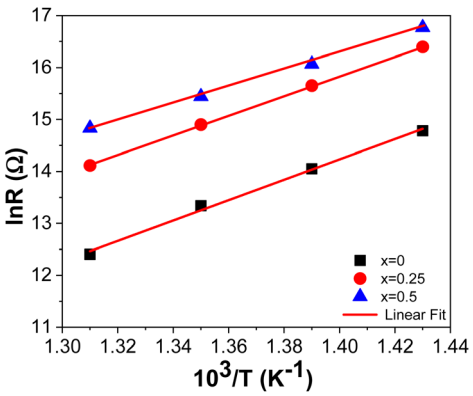

Fig. 10 Evolution of ln R as a function of $10^3/T$ at 1 kHz for BS_xSTN ceramics.

Table 10 Activation energy for BS_xSTN

Compounds	BS_0STN	$BS_{0.25}STN$	$BS_{0.5}STN$
E_a (eV)	1.39	1.34	1.15

Table 9 shows that the grain resistance (R_g) decreases with increasing temperature, and (R_g) increases with the amount of Sr into the tungsten bronze structure, indicating effective conduction within the material. This suggests the presence of thermally activated conduction mechanisms in the grains. Fig. 10 shows the strength variation as a function of $10^3/T$.

Table 10 presents the activation energy values determined for the BS_xSTN ceramics. The grain activation energies decrease with the rate of substitution from 1.39 eV for BS_0STN to 1.15 eV for $BS_{0.5}STN$, within the temperatures range of 340 °C to 400 °C.

The obtained E_a values suggest that oxygen vacancies are involved in the conduction mechanism of BS_xSTN ceramics. Specifically, the activation energy of singly ionized vacancies typically falls within the range of 0.3 to 0.5 eV, while for doubly ionized oxygen vacancies, ranges from 0.6 to 1.2 eV.[14,63,64] Consequently, it can be concluded that the E_a values for all samples are associated with the presence of doubly ionized oxygen vacancies.

4. Conclusion

In this study, oxides with the general formula $(Ba_{1-x}Sr_x)_2SmTi_2Nb_3O_{15}$ ($x = 0$, 0.25, 0.5) were synthesized by solid-state method, which belong to the tetragonal tungsten bronze (TTB) family. Through a structural analysis using room temperature powder X-ray diffraction confirmed a pure TTB structure with the *P4bm* space group. Dielectric measurements conducted at room temperature and 1 kHz indicate that the synthesized compounds exhibit high dielectric constants (ε') ranging from 325 to 570, with low dielectric losses ($\tan\delta$) within the range of 10^{-4} to 10^{-3}. The observed phase transition in these compounds is composition-dependent, with the dielectric constant of $Ba_2SmTi_2Nb_3O_{15}$ significantly higher than that of the Sr-doped compounds. All compounds demonstrated a diffuse-type ferroelectric-to-paraelectric phase transition. The results suggested that the phase transition temperature (T_C) varied in correlation with the atomic displacement of Ti/Nb(1) within the octahedral Ti/NbO_6. The optical transmittance spectra indicate that BS_0STN exhibits higher transparency compared to $BS_{0.25}STN$ and $BS_{0.5}STN$. The optical band gap energies (E_g) for BS_0STN, $BS_{0.25}STN$, and $BS_{0.5}STN$ were determined to be 3.25 eV, 3.56 eV, and 3.59 eV, respectively. Furthermore, as the rate of substitution of Ba by Sr increased, resistance values exhibited an increase, while activation energies of the grains decreased within the temperature range of 340 °C to 400 °C. Nyquists plots indicated an increase in resistance values with the rate of substitution, decreased with increasing temperature. The activation energy, obtained by fitting the Arrhenius formula at high temperatures, decreased within the substitution x from 1.39 to 1.15 eV. This suggests that doubly ionized oxygen vacancies are responsible for electrical conduction in $(Ba_{1-x}Sr_x)_2SmTi_2Nb_3O_{15}$ ceramics.

Conflicts of interest

There are no conflicts to declare.

Acknowledgements

It is to be acknowledged that the Department of Chemistry, Laboratory of Molecular Chemistry, Materials and Environment, at the Faculty Multidisciplinary in Nador (FPN), University Mohammed Premier, helped with the analysis this study needed.

References

1 I.-E. Nylund, C. R. Zeiger, D. Peng, P. E. Vullum, J. Walker, M.-A. Einarsrud and T. Grande, *Chem. Mater.*, 2022, **35**, 17–26.
2 S. Dubey, K. Dubey, V. Sahu, A. Modi, G. Pagare, F. Z. Haque and N. K. Gaur, *J. Mater. Sci.: Mater. Electron.*, 2023, **34**, 2312.
3 E. Cavalli, G. Calestani, E. Bovero, A. Belletti and A. Migliori, *J. Phys.: Condens.Matter*, 2004, **16**, 729.
4 J. Xing, F. Luo, Y. Qin, Y. Luo, Z. Gao, F. Shang and G. Chen, *J. Am. Ceram. Soc.*, 2023, **106**, 1074–1088.
5 X. Zuo, D. Song, Y. Zheng, Z. Hui, T. Guo, W. Dong, E. He, Y. Qin, B. Guan and J. Yang, *Results Phys.*, 2023, 107230.
6 S. Chaudhary, S. Devi and S. Jindal, *Mater. Chem. Phys.*, 2024, **312**, 128580.
7 C. J. Huang, K. Li, X. Q. Liu, X. L. Zhu and X. M. Chen, *J. Am. Ceram. Soc.*, 2014, **97**, 507–512.
8 Y. B. Yao and C. L. Mak, *J. Alloys Compd.*, 2012, **544**, 87–93.
9 S. B. Rao, P. Viswarupachary and D. M. Potukuchi, *Mater. Res. Express*, 2019, **6**, 66562.
10 E. H. Yahakoub, A. Bendahhou, K. Chourti, F. Chaou, I. Jalafi, S. El Barkany, Z. Bahari and M. Abou-salama, *RSC Adv.*, 2022, **12**, 33124–33141.
11 I. Jalafi, A. Bendahhou, K. Chourti, F. Chaou, S. E. L. Barkany and M. Abou-Salama, *Ceram. Int.*, 2023, **49**, 10213–10223.
12 L. Wei, Z. Yang, R. Gu and H. Ren, *J. Am. Ceram. Soc.*, 2010, **93**, 1978–1983.
13 J. Fan, B. Yang, L. Wei and Z. Wang, *Ceram. Int.*, 2016, **42**, 4054–4062.
14 S. Wu, C. Sun, X. Yang, C. Hu, L. Liu and L. Fang, *Ceram. Int.*, 2020, **46**, 9240–9248.
15 Z. Guo, S. Wu, C. Hu, L. Liu and L. Fang, *J. Alloys Compd.*, 2019, **773**, 470–481.
16 K. Chourti, P. Marchet, Y. Elhafiane, A. Bendahhou, S. El barkany, M. Karroua and M. Abou-salama, *Moroccan J. Chem.*, 2020, **8**, 304–317.
17 J. S. Hong, Y. H. Huang, X. Q. Liu, J. Li and Y. J. Wu, *J. Alloys Compd.*, 2019, **770**, 143–148.
18 F. Chaou, I. Jalafi, A. Bendahhou, S. El Barkany and M. Abou-Salama, *Mater. Chem. Phys.*, 2023, **310**, 128426.
19 A. Bendahhou, K. Chourti, F. Chaou, I. Jalafi, S. El Barkany and M. Abou-Salama, *Mater. Res. Bull.*, 2023, **165**, 112319.

20 I. Jalafi, F. Chaou, W. Bouazzati, A. Bendahhou, S. E. L. Barkany and M. Abou-Salama, *J. Solid State Chem.*, 2023, 124506.
21 E. H. Yahakoub, A. Bendahhou, I. Jalafi, F. Chaou, S. EL Barkany, Z. Bahari and M. Abou-Salama, *Heliyon*, 2023, **9**(11), 21037.
22 S. Kamba, S. Veljko, M. Kempa, M. Savinov, V. Bovtun, P. Vaněk, J. Petzelt, M. C. Stennett, I. M. Reaney and A. R. West, *J. Eur. Ceram. Soc.*, 2005, **25**, 3069–3073.
23 X. L. Zhu, X. M. Chen, X. Q. Liu and X. G. Li, *J. Appl. Phys.*, 2009, **105**(12), 124110.
24 M. Prades, H. Beltrán, N. Masó, E. Cordoncillo and A. R. West, *J. Appl. Phys.*, 2008, **104**(10), 104118.
25 X. Zhu and X. Chen, *Appl. Phys. Lett.*, 2010, **96**, 32901.
26 X. H. Zheng and X. M. Chen, *J. Mater. Res.*, 2002, **17**(7), 1664–1670.
27 M. C. Stennett, I. M. Reaney, G. C. Miles, D. I. Woodward, A. R. West, C. A. Kirk and I. Levin, *J. Appl. Phys.*, 2007, **101**, 104114.
28 S. C. Abrahams, S. K. Kurtz and P. B. Jamieson, *Phys. Rev.*, 1968, **172**, 551.
29 M. Paściak, P. Ondrejkovic, J. Kulda, P. Vaněk, J. Drahokoupil, G. Steciuk, L. Palatinus, T. R. Welberry, H. E. Fischer and J. Hlinka, *Phys. Rev. B*, 2019, **99**, 104102.
30 V. Petrícek, M. Dusek and L. Palatinus, *Z. fur Krist.–Cryst. Mater.*, 2014, **229**(5), 345–352.
31 K. Momma and F. Izumi, *J. Appl. Crystallogr.*, 2011, **44**, 1272–1276.
32 P. Scherrer, in *Kolloidchemie Ein Lehrbuch*, Springer, 1912, pp. 387–409.
33 H. M. Rietveld, *J. Appl. Crystallogr.*, 1969, **2**, 65–71.
34 Z. Chchiyai, F. El Bachraoui, Y. Tamraoui, L. Bih, A. Lahmar, M. El Marssi, J. Alami and B. Manoun, *J. Alloys Compd.*, 2022, **927**, 166979.
35 R. D. Shannon, *Acta Crystallogr., Sect. A*, 1976, **32**, 751–767.
36 M. Arshad, H. Du, M. S. Javed, A. Maqsood, I. Ashraf, S. Hussain, W. Ma and H. Ran, *Ceram. Int.*, 2020, **46**, 2238–2246.
37 W. Huang, X. Du, S. K. Thatikonda, N. Qin, C. Yao, A. Hao and D. Bao, *Ceram. Int.*, 2019, **45**, 10475–10480.
38 J. Ruiz-Fuertes, O. Gomis, A. Segura, M. Bettinelli, M. Burianek and M. Mühlberg, *Appl. Phys. Lett.*, 2018, **114**(4), DOI: 10.1063/1.5012111.
39 A. R. F. Lima, J. C. Sczancoski, M. S. Li, E. Longo and E. R. Camargo, *Ceram. Int.*, 2016, **42**, 4709–4714.
40 D. Fan, R. Chong, F. Fan, X. Wang, C. Li and Z. Feng, *Chin. J. Catal.*, 2016, **37**, 1257–1262.
41 L. L. G. Al-mahamad, *Heliyon*, 2022, **8**, e09966.
42 T. Badapanda, S. Sarangi, B. Behera, S. Parida, S. Saha, T. P. Sinha, R. Ranjan and P. K. Sahoo, *J. Alloys Compd.*, 2015, **645**, 586–596.
43 A. O. Turky, M. M. Rashad, A. M. Hassan, E. M. Elnaggar and M. Bechelany, *Phys. Chem. Chem. Phys.*, 2017, **19**, 6878–6886.
44 A. Kumawat, S. Chattopadhyay, K. P. Misra, N. Halder, S. K. Jain and B. L. Choudhary, *Solid State Sci.*, 2020, **108**, 106379.
45 M. Rouchdi, E. Salmani, B. Fares, N. Hassanain and A. Mzerd, *Results Phys.*, 2017, **7**, 620–627.
46 B. G. Hunashimarad, J. S. Bhat, P. V Raghavendra and R. F. Bhajantri, *Opt. Mater.*, 2021, **114**, 110962.
47 R. GopalaraoTanguturi, T. Bora, S. Ravi and D. Pamu, *Phys. Procedia*, 2014, **54**, 70–74.
48 I. Jalafi, A. Bendahhou, K. Chourti, F. Chaou, S. El Barkany and M. Abou-Salama, *Ceram. Int.*, 2023, **49**(7), 10213–10223.
49 X. M. Chen, Y. H. Sun and X. H. Zheng, *J. Eur. Ceram. Soc.*, 2003, **23**, 1571–1575.
50 C. Hu, X. Peng, L. Fang, C. Li and B. Wu, *J. Wuhan Univ. Technol., Mater. Sci. Ed.*, 2011, **26**, 311.
51 X. M. Chen and J. S. Yang, *J. Eur. Ceram. Soc.*, 1999, **19**, 139–142.
52 S. M. Pilgrim, A. E. Sutherland and S. R. Winzer, *J. Am. Ceram. Soc.*, 1990, **73**, 3122–3125.
53 I. W. Kim, C. W. Ahn, J. S. Kim, T. K. Song, J.-S. Bae, B. C. Choi, J.-H. Jeong and J. S. Lee, *Appl. Phys. Lett.*, 2002, **80**, 4006–4008.
54 G. A. Smolenskii, *J. Phys. Soc. Jpn.*, 1970, **28**, 26–37.
55 P. Ganguly and A. K. Jha, *Phys. B*, 2010, **405**, 3154–3158.
56 C. K. Suman, K. Prasad and R. N. P. Choudhary, *J. Mater. Sci.*, 2006, **41**, 369–375.
57 F. A. Kröger and H. J. Vink, in *Solid State Physics*, Elsevier, 1956, Vol. 3, pp. 307–435.
58 J. R. Macdonald, Impedance spectroscopy, *Ann. Biomed. Eng.*, 1992, **20**, 289–305.
59 H. Ali, S. Karim, M. A. Rafiq, K. Maaz, A. U. Rahman, A. Nisar and M. Ahmad, *J. Alloys Compd.*, 2014, **612**, 64–68.
60 S. Rani, N. Ahlawat, R. Punia, K. M. Sangwan and P. Khandelwal, *Ceram. Int.*, 2018, **44**, 23125–23136.
61 H. Ma, K. Lin, L. Fan, Y. Rong, J. Chen, J. Deng, L. Liu, S. Kawaguchi, K. Kato and X. Xing, *RSC Adv.*, 2015, **5**, 71890–71895.
62 J. R. Macdonald, *J. Appl. Phys.*, 1985, **58**, 1955–1970.
63 X. Sun, J. Deng, L. Liu, S. Liu, D. Shi, L. Fang and B. Elouadi, *Mater. Res. Bull.*, 2016, **73**, 437–445.
64 K. Kumari, A. Prasad and K. Prasad, *Am. J. Mater. Sci.*, 2016, **6**, 1–18.